The University of Osaka
Institutional Knowledge Archive

Title	Design and fabrication of Ti-Zr-Hf-Cr-Mo and Ti-Zr-Hf-Co-Cr-Mo high-entropy alloys as metallic biomaterials
Author(s)	Nagase, Takeshi; Iijima, Yuuka; Matsugaki, Aira et al.
Citation	Materials Science and Engineering C. 2020, 107, p. 110322
Version Type	VoR
URL	https://hdl.handle.net/11094/89809
rights	This article is licensed under a Creative Commons Attribution 4.0 International License.
Note	

The University of Osaka Institutional Knowledge Archive : OUKA

https://ir.library.osaka-u.ac.jp/

The University of Osaka

Materials Science & Engineering C 107 (2020) 110322

Contents lists available at ScienceDirect

Materials Science & Engineering C

journal homepage: www.elsevier.com/locate/msec

Design and fabrication of Ti–Zr-Hf-Cr-Mo and Ti–Zr-Hf-Co-Cr-Mo high-entropy alloys as metallic biomaterials

Takeshi Nagase[a,b], Yuuka Iijima[b], Aira Matsugaki[b], Kei Ameyama[c], Takayoshi Nakano[b,*]

[a] Research Center for Ultra-High-Voltage Electron Microscopy, Osaka University, 7-1, Mihogaoka, Ibaraki, Osaka, 567-0047, Japan
[b] Division of Materials and Manufacturing Science, Graduate School of Engineering, Osaka University, 2-1, Yamadaoka, Suita, Osaka, 565-0871, Japan
[c] Department of Mechanical Engineering, Ritsumeikan University, 1-1-1 Noji-higashi, Kusatsu, Shiga, 525-8577, Japan

ARTICLE INFO

Keywords:
Biomaterials
High-entropy alloys
Alloy design

ABSTRACT

Novel $TiZrHfCr_{0.2}Mo$ and $TiZrHfCo_{0.07}Cr_{0.07}Mo$ high-entropy alloys for metallic biomaterials (bio-HEAs) were developed based on the combination of Ti–Nb–Ta–Zr–Mo alloy system and Co–Cr–Mo alloy system as commercially-used metallic biomaterials. Ti–Zr-Hf-Cr-Mo and Ti–Zr-Hf-Co-Cr-Mo bio-HEAs were designed using (a) a tree-like diagram for alloy development, (b) empirical alloy parameters for solid-solution-phase formation, and (c) thermodynamic calculations focused on solidification. The newly-developed bio-HEAs overcomes the limitation of classical metallic biomaterials by the improvement of (i) mechanical hardness and (ii) biocompatibility all together. The $TiZrHfCr_{0.2}Mo$ and $TiZrHfCo_{0.07}Cr_{0.07}Mo$ bio-HEAs showed superior biocompatibility comparable to that of commercial-purity Ti. The superior biocompatibility, high mechanical hardness and low liquidus temperature for the material processing in $TiZrHfCr_{0.2}Mo$ and $TiZrHfCo_{0.07}Cr_{0.07}Mo$ bio-HEAs compared with the Ti–Nb–Ta–Zr–Mo bio-HEAs gave the authenticity of the application of bio-HEAs for orthopedic implants with multiple functions.

1. Introduction

Development of a new generation of metallic biomaterials possessing both biocompatibility and good mechanical properties is necessary for satisfying the demands of future medical applications. Recently, a new class of structural and functional materials, labeled high-entropy alloys (HEAs), was developed [1–14]. Our group developed HEAs for use as metallic biomaterials (hereafter called bio-HEAs), e.g., equiatomic TiNbTaZrMo HEA [15–17]; non-equiatomic $Ti_{2.6}NbTaZrMo$ HEA [16]; and $Ti_{1.4}Zr_{1.4}Nb_{0.6}Ta_{0.6}Zr_{0.6}$, $Ti_{1.7}NbTaZrMo_{0.5}$, and $Ti_{1.5}NbTaZrMo_{0.5}$ HEAs [18]. Wang et al. examined the application of the TiNbTaZrMo bio-HEA to orthopedic implants [19]. Yuan et al. reported the structure and properties of biocompatible TiZrHfNbTa and related bio-HEAs and bio-medium entropy alloys (MEAs) including alloy design for low Young's modulus [20]. Motallebzadeh et al. reported the microstructural, mechanical and electrochemical characterization of TiZrHfNbTa and $Ti_{1.5}ZrTa_{0.5}Hf_{0.5}Nb_{0.5}$ bio-HEAs for biomedical applications [21]. Popescu et al. developed TiZrNbTaFe bio-HEAs for medical applications [22]. TiNbTaZr MEAs without toxic elements were reported to show the strong BCC solid solution formation tendency and the superior ductility [15,23]. The constituent elements of bio-HEAs are similar to those of RHEAs [24–30]; however, the concepts of alloy design and the desired mechanical and functional properties differ significantly between bio-HEAs and RHEAs. In bio-HEAs, the biocompatibility of the constituent elements is the most important factor for alloy design.

Co–Cr and Co–Cr–Mo alloys are commonly accepted metallic biomaterials [31–36], as well as titanium-based alloys, particularly for surgical implants and dental alloys such as ASTM F75 [37], ASTM F1537 [38], and JIS T 7402 [39]. They are now widely used as sliding materials in artificial joints [40]. As previously noted, we recently reported the novel advantages of Ti–Nb–Ta–Zr–Mo HEAs as biomaterials. The $Ti_{1.4}Nb_{0.6}Ta_{0.6}Zr_{1.4}Mo_{0.6}$ bio-HEAs show excellent molecular interactions between cells and HEAs with the formation of elongated mature fibrillar adhesions [18]. This finding leads us to hypothesize the good performance of bio-HEAs containing Co and Cr as biomedical materials. In the present study, the combination of the Ti–Nb–-Ta–Zr–Mo and Co–Cr–Mo alloy systems for the development of a new alloy system of bio-HEAs was investigated. The similarity in the constituent element in the bio-HEAs and RHEAs leads to the high liquidus temperature (T_L) for bio-HEAs without the Co and Cr elements. A high T_L may be favorable for RHEAs; however, bio-HEAs do not typically exhibit such a property. A significantly high T_L is a hindrance to the fabrication of bio-HEAs, and it increases the fabrication cost. A low T_L

* Corresponding author.
E-mail address: nakano@mat.eng.osaka-u.ac.jp (T. Nakano).

https://doi.org/10.1016/j.msec.2019.110322
Received 6 August 2019; Received in revised form 19 September 2019; Accepted 14 October 2019
Available online 22 October 2019
0928-4931/ © 2019 The Authors. Published by Elsevier B.V. This is an open access article under the CC BY license (http://creativecommons.org/licenses/BY/4.0/).

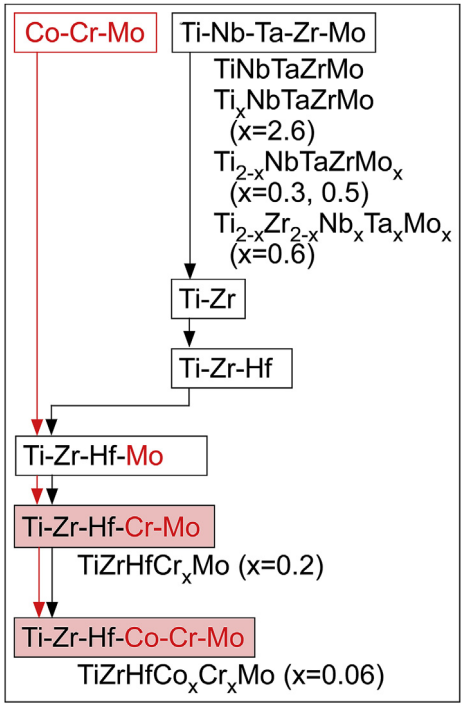

Fig. 1. Alloy design using treelike diagram of evolution of TiZrHfCr$_x$Mo and TiZrHfCo$_x$Cr$_x$Mo bio-HEAs.

can overcome these problems and enable significantly more cost-effective production of bio-HEAs. Specifically, a decrease in T_L below 2273 K (2000 °C) is one of the important objectives for overcoming the above-stated problems in the fabrication of bio-HEAs from an engineering standpoint. The combination of Ti–Nb–Ta–Zr–Mo bio-HEAs and the castable Co–Cr–Mo alloys for metallic biomaterials was considered to be effective to decrease T_L. This paper reports on the design and development of TiZrHfCr$_x$Mo and TiZrHfCo$_x$Cr$_x$Mo bio-HEAs with superior biocompatibility comparable to that of CP-Ti, both of whose T_L values are estimated to be below 2273 K, where TiZrHfCr$_x$Mo and TiZrHfCo$_x$Cr$_x$Mo bio-HEAs were constructed using biocompatible elements.

2. Alloy design

Ti–Nb–Ta–Zr–Mo was the starting alloy system of the bio-HEAs [15–19]. Fig. 1 shows the design of the bio-HEAs using the treelike diagram. The following strategy was adopted for selection of the constituent elements using the treelike diagram for the combination of the Ti–Nb–Ta–Zr–Mo and Co–Cr–Mo alloy systems. (1) High-melting-temperature elements, i.e. Nb, Mo, and Ta, were removed from Ti–Nb–Ta–Zr–Mo, which yielded Ti–Zr. (2) Subsequently, Hf was added to Ti–Zr. Hf is a metallic element with good biocompatibility and osteogenesis, as confirmed by an animal implantation test [41]. Hf has also been used as one of the additive elements in Ti-based metallic biomaterials [42,43]. Furthermore, Hf-containing bio-HEAs have been reported previously [20,21]. Sheikh et al. reported that a decrease in the number of valence electrons through controlled alloying based on the valence electron concentration (VEC) theory was effective for achieving intrinsic ductility of RHEAs [44]. Yuan et al. reported that the decrease in VEC was also effective to decrease the Young's modulus of bio-HEAs [20]. The addition of Hf can be considered an effective strategy for realizing bio-HEAs with room-temperature ductility and low Young's modulus. The Ti–Zr–Hf alloy system was designed via the addition of Hf to Ti–Zr. (3) As the third step, Nb and Mo were considered as candidate elements for bio-HEAs. The melting temperature of Mo (2896 K) is higher than that of Nb (2741 K). Recent reports regarding the development of Ti–Nb-based multicomponent alloys [45–47] and additive manufacturing in Ti-based alloys [47–49] may imply that Nb is preferable over Mo. However, Mo was selected in the present study because of the combination of the Co–Cr–Mo alloy system, resulting in a Ti–Zr-Hf-Mo alloy system. (4) Co and Cr were selected as promising additive elements for the consideration, the resulting five-component Ti–Zr–Hf–Co–Mo and Ti–Zr–Hf–Cr–Mo and six-component Ti–Zr–Hf–Co–Cr–Mo alloy systems were considered promising candidates for bio-HEAs without toxic elements. (5) Further discussion of the alloy system was made based on the empirical alloy parameters for the prediction of the solid-solution phases in HEAs. The parametric approach was effective for a rough design analysis of the newly developed Ti–Nb–Ta–Zr–Mo bio-HEAs [15]. In this study, the possibility for the solid solution phase formation in the 5-component Ti–Zr–Hf–Co–Mo and Ti–Zr–Hf–Cr–Mo and 6-component Ti–Zr–Hf–Co–Cr–Mo alloy systems was discussed based on the empirical alloy parameters including following empirical parameters: mixing entropy ΔS_{mix} [8,9]; mixing enthalpy ΔH_{mix} [8,9]; a parameter for evaluating the difference in the atomic radii of the constituent elements, δ [8,9], and a dimensionless parameter Ω, which was calculated using both ΔS_{mix} and ΔH_{mix} [8,9,50]. The mixing enthalpy ΔH_{i-j} calculated by the Miedema's model for i–j atomic pairs and atomic radii of the i elements r_i are important parameters for the calculation of ΔH_{mix}, δ, and Ω. Fig. 2 shows the values of ΔH_{i-j} for i–j atomic pairs and atomic radii of the i elements r_i in the Ti–Zr–Hf–Co–Cr–Mo alloy system, obtained from Ref. [51]. In the map of ΔH_{i-j} (Fig. 2a), the pairs of Co–Ti (−28), Co–Zr (−41), and Co–Hf (−35) exhibited large negative values. This indicates that the addition of Co in Ti–Zr–Hf–Mo alloys are undesirable for HEAs, based on the ΔH_{mix} and Ω parameters. For a five-component alloy system for bio-HEAs, Ti–Zr–Hf–Cr–Mo alloys were selected in the present study. (6) Based on the parametric approach concerning ΔH_{i-j}, Co was not a suitable additional element for the Ti–Zr–Hf–Mo alloys. In contrast, the addition of both Co and Cr in the Ti–Zr–Hf–Mo alloys significantly and effectively increased ΔS_{mix}. A difference in r_i was not seen between Co and Cr (Fig. 2b). For a six-component alloy system for bio-HEAs, Ti–Zr–Hf–Co–Cr–Mo alloys were also investigated in the present study.

Based on the above-described discussion, the five-component Ti–Zr–Hf–Cr–Mo and six-component Ti–Zr–Hf–Co–Cr–Mo alloy systems were considered. In the map of the atomic radii of the i elements r_i (Fig. 2b), the atomic radii of Co and Cr are significantly smaller than those of Ti, Zr, and Hf. The increase in Cr concentration in Ti–Zr–Hf–Cr–Mo alloy and that of Co and Cr concentration in Ti–Zr–Hf–Co–Cr–Mo alloys lead to an increase in δ, which is not favorable for the formation of the solid solution phase. The increase in Co

(a) ΔH_{i-j} [kJ/mol]

	Ti	Zr	Hf	Co	Cr	Mo
Ti		0	0	-28	-7	-4
Zr			0	-41	-12	-6
Hf				-35	-9	-4
Co					-4	-5
Cr						-6
Mo						

(b) r_{i-j} [nm]

Ti	0.147	Co	0.125
Zr	0.162	Cr	0.125
Hf	0.16	Mo	0.136

Fig. 2. (a) Mixing enthalpy ΔH_{i-j} calculated by the Miedema's model for i–j atomic pairs. and (b) atomic radii of the i elements r_i. These data were obtained from Ref. [51].

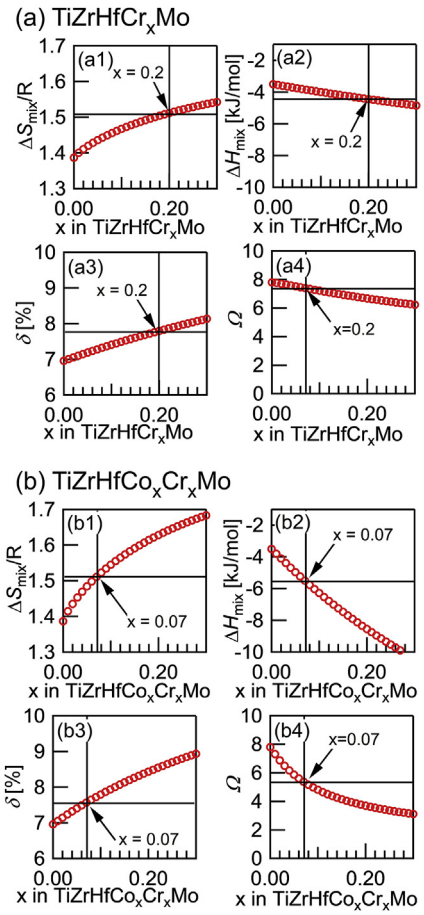

Fig. 3. Empirical alloy parameters for prediction of the solid solution phases in the $TiZrHfCr_xMo$ and $TiZrHfCo_xCr_xMo$ bio-HEAs. (a) $TiZrHfCr_xMo$. (b) $TiZrHfCo_xCr_xMo$. (a1)(b1) $\Delta S_{mix}/R$, (a2)(b2) ΔH_{mix}, (a3)(b3) δ [%], (a4)(b4) Ω.

in Ti–Zr–Hf–Co–Cr–Mo alloys was not suitable for ΔH_{mix} parameters because of the large negative $\Delta H_{i\text{–}j}$ values of Co–Ti (−28), Co–Zr (−41), and Co–Hf (−35) (Fig. 2a). Finally, the 5-component $TiZrHfCr_xMo$ ($x \geq 0$) and 6-component $TiZrHfCo_xCr_xMo$ ($x \geq 0$) alloys were investigated in this study. In the alloy map (Fig. 2), the alloy compositions of $TiZrHfCr_xMo$ and $TiZrHfCo_xCr_xMo$ are presented together with the alloy system.

Fig. 3 shows the empirical alloy parameters for prediction of the solid solution phases in the $TiZrHfCr_xMo$ and $TiZrHfCo_xCr_xMo$ alloys. $\Delta S_{mix}/R$ of the $TiZrHfCr_xMo$ and $TiZrHfCo_xCr_xMo$ alloys are shown in Fig. 3a1 and 3b1, respectively. The increase in x leads to an increase in ΔS_{mix} for both $TiZrHfCr_xMo$ and $TiZrHfCo_xCr_xMo$ alloys. The minimum values to satisfy $\Delta S_{mix}/R \geq 1.5R$ were $x = 0.2$ for the $TiZrHfCr_xMo$ alloys and $x = 0.07$ for the $TiZrHfCo_xCr_xMo$ alloys. The values of ΔH_{mix} of the $TiZrHfCr_xMo$ (Fig. 3a2) and $TiZrHfCo_xCr_xMo$ (Fig. 3b2) alloys were negative; their absolute values increased with x, which indicates that the increase in x was not favorable for the formation of HEAs considering the interactions of the constituent elements. However, the ΔH_{mix} values imply the high solid solution tendency in the $TiZrHfCr_xMo$ and $TiZrHfCo_xCr_xMo$ alloys with $x \leq 0.3$ owing to the low absolute values of ΔH_{mix}. The values of δ of the $TiZrHfCr_xMo$ (Fig. 3a3) and $TiZrHfCo_xCr_xMo$ (Fig. 3b3) alloys increased with x, which indicates that the increase in x was not favorable for the formation of HEAs considering the difference in atomic radius between the constituent elements. The values of δ of the $TiZrHfCr_xMo$ and $TiZrHfCo_xCr_xMo$ alloys were higher than those of the typical RHEAs [7,8,28]. The values of δ of the $TiZrHfCr_{0.2}Mo$ ($TiZrHfCo_xMo$, $x = 0.2$) and $TiZrHfCo_{0.07}Cr_{0.07}Mo$ ($TiZrHfCo_xCr_xMo$, $x = 0.07$) alloys, where x had the minimum value satisfying $\Delta S_{mix}/R \geq 1.5R$, were 7.8 and 7.6, respectively. The large δ values of the $TiZrHfCr_xMo$ and $TiZrHfCo_xCr_xMo$ alloys indicate that the increases in the concentrations of Co and Cr had negative effects on the formation of the solid solution. The x values should be minimum to suppress the intermetallic compound formation due to the atomic size effect. The Ω parameters of the $TiZrHfCr_xMo$ (Fig. 3a4) and $TiZrHfCo_xCr_xMo$ (Fig. 3b4) alloys decreased with the increase in x. The Co- and Cr-concentration dependence of Ω was mainly attributed to the increase in the absolute value of ΔH_{mix} with the increase in x. The values of Ω of the $TiZrHfCr_xMo$ and $TiZrHfCo_xCr_xMo$ alloys for $0 \leq x \leq 0.3$ were larger than 1.1, which indicates the high solid-solution formation tendency in the $TiZrHfCr_xMo$ and $TiZrHfCo_xCr_xMo$ alloys for $0 \leq x \leq 0.3$.

As denoted in the review paper [14], it's found in a number of these alloys, and the exploration of alloys containing this phase could be accelerated using the CALculated PHAse Diagram (CALPHAD) method. The pseudo-binary phase diagrams constructed using only the Gibbs free energies of a single liquid phase and single BCC phase were effective to estimate T_L and evaluate the solidification microstructures in Ti–Nb–Ta–Zr–Mo bio-HEAs [16,17,52]. A thermodynamic calculation focused on T_L was performed for the $TiZrHfCr_xMo$ and $TiZrHfCo_xCr_xMo$ alloys for $0 \leq x \leq 0.3$. Fig. 4 shows the pseudo-binary phase diagrams focused on T_L [K] estimated from thermodynamic calculations considering a single liquid phase and single BCC phase. The thermodynamic calculations were performed with FactSage (ver. 7.3) using the thermodynamic databases for alloy systems from Scientific Group Thermodata Europe (SGTE) 2017 [53]. T_L of the equiatomic TiZrHfMo alloy was estimated to be 1995 K, which is much lower than 2273 K (2000 °C). T_L (red solid line) monotonously decreased with increasing x and y of the $TiZrHfCr_xMo$ (Fig. 4a1) and $TiZrHfCo_yCr_yMo$ (Fig. 4a2) alloys, respectively. The $TiZrHfCr_{0.2}Mo$ ($TiZrHfCr_xMo$, $x = 0.2$) and $TiZrHfCo_{0.07}Cr_{0.07}Mo$ ($TiZrHfCo_yCr_yMo$, $y = 0.07$) bio-HEAs were designed on the basis of these thermodynamic calculation results; these x and y values were the minimum values that satisfied an entropy-based definition of HEAs, i.e., $\Delta S_{mix}/R \geq 1.5R$ [8,9]. The T_L values of the $TiZrHfCr_{0.2}Mo$ (1978 K, 1705 °C) and $TiZrHfCo_{0.07}Cr_{0.07}Mo$ (1980 K, 1707 °C) alloys were lower than 2273 K (2000 °C) and significantly lower than that of equiatomic TiNbTaZrMo (2484 K, 2211 °C;

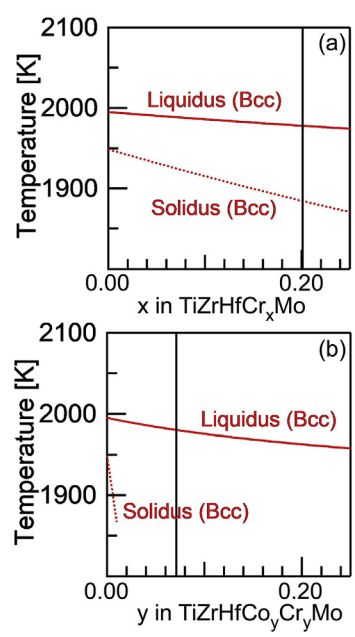

Fig. 4. Pseudo-binary phase diagrams focused on the liquidus temperature T_L [K] and solidus temperature T_S [K] estimated from thermodynamic calculations considering a single BCC phase and single liquid phase. (a) $TiZrHfCr_xMo$ and (b) $TiZrHfCo_xCr_xMo$.

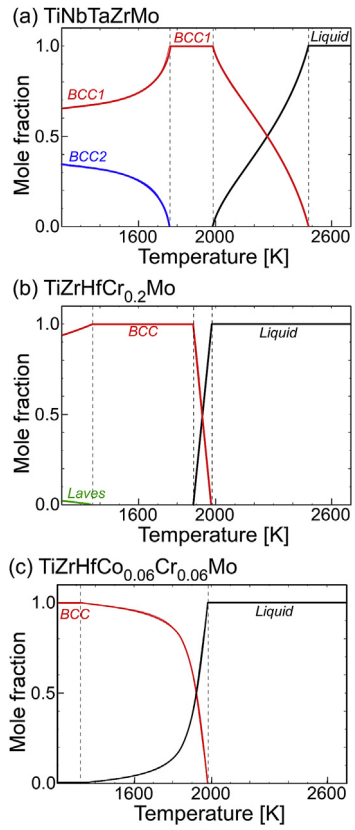

Fig. 5. Equilibrium calculation results of equiatomic TiNbTaZrMo (a), $TiZrHfCr_{0.2}Mo$ (b) and $TiZrHfCo_{0.07}Cr_{0.07}Mo$ (c) bio-HEAs.

SGTE2017) [16,52].

Fig. 5 shows thermodynamic equilibrium calculation results of equiatomic TiNbTaZrMo (a), $TiZrHfCr_{0.2}Mo$ (b) and $TiZrHfCo_{0.07}Cr_{0.07}Mo$ (c) bio-HEAs. The equilibrium calculation of $TiZrHfCr_{0.2}Mo$ (Fig. 5b) and $TiZrHfCo_{0.07}Cr_{0.07}Mo$ (Fig. 5c) showed that the BCC phase forms first during cooling of liquid and the T_L was much lower than that of equiatomic TiNbTaZrMo. BCC single phase region was observed in equiatomic TiNbTaZrMo (Fig. 5a), $TiZrHfCr_{0.2}Mo$ (Fig. 5b) and $TiZrHfCo_{0.07}Cr_{0.07}Mo$ (Fig. 5c), regardless the alloy system. The BCC phase decomposed to dual BCC phases in equiatomic TiNbTaZrMo (Fig. 5a), and this was discussed in detail in the literature [15]. The minor laves phase was found at the temperature below about 1500 K in $TiZrHfCr_{0.2}Mo$ (Fig. 5b). The wide solid (BCC)-liquid co-existing temperature range was observed in $TiZrHfCo_{0.07}Cr_{0.07}Mo$ (Fig. 5c). It should be noted here that single BCC phase was stable at the temperature just below T_S in $TiZrHfCr_{0.2}Mo$ (Fig. 5b) and $TiZrHfCo_{0.07}Cr_{0.07}Mo$ (Fig. 5c) bio-HEAs. Table 1 summarized the thermodynamic calculation results of liquidus temperatures T_L [K] and distribution coefficient (k) at T_L in $TiZrHfCr_xMo$ and $TiZrHfCo_xCr_xMo$ HEAs. The value of k in Zr and Cr was lower that the unity in $TiZrHfCr_xMo$ (Table 1a) and $TiZrHfCo_xCr_xMo$ (Table 1b) bio-HEAs. The value of k in Co was significantly lower than the unity in $TiZrHfCo_xCr_xMo$ (Table 1b), indicating that the solubility limit of Co in BCC phase was significantly small and Co was enriched in the residual liquid during solidification in $TiZrHfCo_xCr_xMo$ resulting in the wide solid (BCC)-liquid co-existing temperature range. Based on the treelike diagram (Fig. 1), empirical alloy parameters (Figs. 2 and 3), and thermodynamic calculations (Figs. 4 and 5, **and** Table 1), $TiZrHfCr_{0.2}Mo$ ($TiZrHfCo_xMo$, $x = 0.2$) and $TiZrHfCo_{0.07}Cr_{0.07}Mo$ ($TiZrHfCo_xCr_xMo$, $x = 0.07$) bio-HEAs were designed.

Table 1
Thermodynamic calculation results of liquidus temperatures T_L [K] and distribution coefficient at T_L (k) in $TiZrHfCr_xMo$ and $TiZrHfCo_xCr_xMo$ HEAs.

(a) $TiZrHfCr_xMo$

x	T_L	k at T_L					
	[K]	Ti	Zr	Hf	Co	Cr	Mo
0.00	1995	0.96	0.69	1.07			1.28
0.07	1994	0.96	0.67	1.08		0.63	1.31
0.10	1986	0.97	0.66	1.09		0.63	1.32
0.20	1978	0.97	0.63	1.11		0.64	1.36

(b) $TiZrHfCo_xCr_xMo$

x	T_L	k at T_L					
	[K]	Ti	Zr	Hf	Co	Cr	Mo
0.07	1980	0.98	0.59	1.06	0.05	0.66	1.45
0.10	1975	0.99	0.55	1.06	0.05	0.68	1.53
0.20	1963	1.01	0.44	1.04	0.04	0.73	1.76

3. Experimental procedures

Arc-melted ingots of the $TiZrHfCr_{0.2}Mo$ and $TiZrHfCo_{0.07}Cr_{0.07}Mo$ alloys were prepared in an arc-melting furnace (ACM-S01, Diavac, Japan) from a mixture of pure-element lumps. Ti chips (purity: 3 N), Zr wire-cut products (purity: 3 N), and Hf sponges ((Hf + Zr) purity: minimum 99.6%), Cr shots (purity: 3 N), Co shots (purity: 3 N), and Mo shots (purity: 3 N) were used as pure-element lumps. In order to achieve homogeneous distributions of the constituent elements in the alloys, the alloy ingots were melted more than 10 times and maintained in a liquid state for approximately 120 s during each melting cycle. The cooling rate during the arc-melting process was approximately 2×10^3 K/s [16,54]. X-ray diffraction (XRD) analysis was performed using a Rigaku (Japan) RINT-2500 X-ray diffractometer with Cu-K_α radiation to identify the constituent phases. The solidification microstructures of the arc-melted ingots of the $TiZrHfCr_{0.2}Mo$ and $TiZrHfCo_{0.07}Cr_{0.07}Mo$ alloys were investigated using scanning electron microscopy (SEM)-back-scattered electron (BSE) imaging. A thermionic-emission gun type SEM equipment with a W filament, the JEM-5600 (JEOL, Japan), was used. The solidification microstructures were also investigated using electron probe microanalysis with wavelength-dispersive spectroscopy (EPMA-WDS). A thermionic-emission gun type EPMA equipment with a W filament, the JXA-8800R (JEOL, Japan), was used. A Vickers micro-hardness (Hv) test was performed with a load of 1.0 kgf using an MVK-E instrument (Akashi Seisakusho, Japan). The values of Hv were the average values of at least 10 positions, in which each position was randomly selected. The specimens for cell cultivation experiments aimed at evaluation of cellular compatibility were prepared by cutting into ϕ9 mm × 1 mm pieces using an electron discharge machining. The surfaces of these substrates were mechanically polished with SiC waterproof papers up to #4000 grit. Prior to the cell cultivation experiments, these specimens were washed with acetone and ethanol in ultrasonication and then placed individually into a 48-well microplate (IWAKI) ($n = 5$). Mouse primary osteoblasts were isolated from neonatal pups calvariae by sequential collagenase/trypsin digestion procedure. The obtained cells were diluted to 10000 cells/cm^2 and seeded onto the substrates. After cultivation for 24 h in a 5% CO_2 humidified atmosphere, the cells were fixed with methanol and stained with a 5% Giemsa aqueous solution (FUJIFILM Wako Chemicals). The cell density cultivated on the substrates was analyzed from optical microscopy (BX60, Olympus) images. The cell adhesion behaviors were evaluated by immunocytochemistry. After cultivation for 24 h, the cells were fixed in 4% paraformaldehyde, followed by washing in phosphate-buffered saline (PBS) with Triton X-100 and immersed in normal goat serum

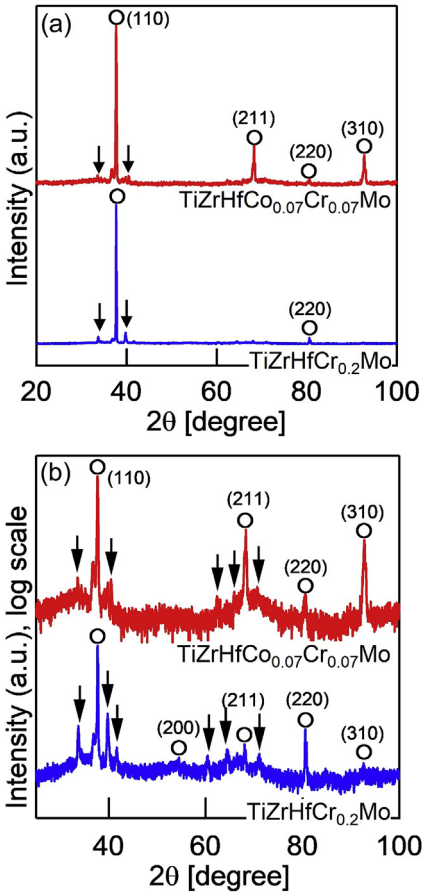

Fig. 6. XRD patterns of the arc-melted ingots of $TiZrHfCr_{0.2}Mo$ and $TiZrHfCo_{0.07}Cr_{0.07}Mo$ bio-HEAs. (a) linear scale plot, (b) log-scale plot.

solution for blockade of non-specific antibody interaction. Then, the cells were incubated with anti-vinculin antibodies (Sigma) and subsequently with secondary antibodies (Alexa Fluor 594 goat anti mouse IgG (Thermo Fisher Scientific) and Alexa Fluor 488 phalloidin (Thermo Fisher Scientific)). The images were observed with fluorescent microscopy (BZ-X710, Keyence). The data were expressed as mean ± standard deviation. The statistical significance was assessed using one-way ANOVA followed by Tukey's post-hoc test. A significance of $p < 0.05$ was required to reject the null hypothesis. In the present study, a microstructure analysis and an evaluation of biocompatibility and mechanical properties were performed for same-batch ingots; most portions of the specimens were used for the biocompatibility test.

4. Results and discussion

Fig. 6 shows XRD patters of the arc-melted ingots of the $TiZrHfCr_{0.2}Mo$ and $TiZrHfCo_{0.07}Cr_{0.07}Mo$ bio-HEAs. A log-scale intensity plot (Fig. 6b) is shown for enhancing the minor peaks. In the linear-scale plot (Fig. 6a), all the high-intensity peaks in the XRD patterns can be indexed as the BCC phase, as indicated by the open circles (○). The lattice constant of the BCC phase estimated from the positions of the intensity peaks in the XRD patterns was 0.337 nm for the $TiZrHfCr_{0.2}Mo$ alloy and 0.336 nm for the $TiZrHfCo_{0.07}Cr_{0.07}Mo$ alloy. Some minor peaks, which were not indexed as the BCC phase, were observed in the ingots of both the $TiZrHfCr_{0.2}Mo$ bio-HEA and the $TiZrHfCo_{0.07}Cr_{0.07}Mo$ bio-HEA, as indicated by the black arrows (Fig. 6a and b). These minor peaks were considered to correspond to Co- and/or Cr-containing Laves-based intermetallic compounds. The number and intensities of the minor peaks corresponding to a non-BCC solid-solution phase in the $TiZrHfCo_{0.07}Cr_{0.07}Mo$ were smaller than those of the $TiZrHfCr_{0.2}Mo$.

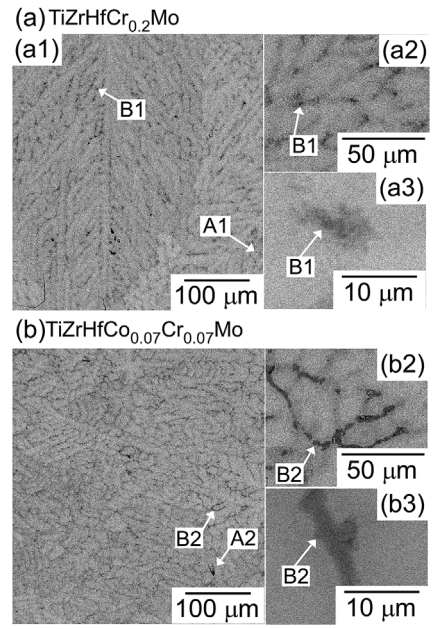

Fig. 7. SEM-BSE images of the as-cast $TiZrHfCr_{0.2}Mo$ and $TiZrHfCo_{0.07}Cr_{0.07}Mo$ bio-HEAs. The inset shows a magnified image focused on the inter-dendrite region. (a) $TiZrHfCr_{0.2}Mo$ and (b) $TiZrHfCo_{0.07}Cr_{0.07}Mo$. (a2) and (a3) are the magnified images of (a1). (b2) and (b3) are the magnified images of (b1).

Fig. 7 shows SEM-BSE images of the arc-melted ingots of the $TiZrHfCr_{0.2}Mo$ and $TiZrHfCo_{0.07}Cr_{0.07}Mo$ bio-HEAs. The black-contrast regions denoted as A1 and A2 were randomly distributed in both as-cast alloys, which could be attributed to the abrasive grains from the SiC abrasive paper as polishing artifacts [55]. Both as-cast $TiZrHfCr_{0.2}Mo$ (Fig. 7a) and $TiZrHfCo_{0.07}Cr_{0.07}Mo$ (Fig. 7b) showed dendritic structures with white–gray-contrast dendrites and dark-gray-contrast inter-dendrite regions (denoted as B1 and B2, respectively). The dendritic structure indicates the redistribution of the constituent elements during the solidification, leading to the formation of a mixture of a main dendrite phase and minor phase corresponding to the inter-dendrite region (B1 and B2). A typical example of the minor phase (B1 and B2) is shown in the magnified image. In the $TiZrHfCr_{0.2}Mo$ bio-HEA, the microstructure of the inter-dendrite region (Fig. 7a2 and 7**a3**) may be a eutectic-like structure; however, formation of the eutectic structure cannot be irrefutably concluded because of the lack of spatial resolution of the thermionic-emission gun type SEM used in the present study. Notably, observation of the solidification microstructure of HEAs using SEM-BSE imaging was difficult for some HEAs because of the complexity of the constituent elements [56]. The unique nature of HEAs in terms of this complexity resulted in difficulty in evaluating the microstructure in the $TiZrHfCr_{0.2}Mo$ HEA in the present study. The clear eutectic-like structure formation was not observed in the inter-dendrite region of the $TiZrHfCo_{0.07}Cr_{0.07}Mo$ bio-HEA (Fig. 7b2 and 7b3). The equiaxial dendrite structure formations in the as-cast $TiZrHfCr_{0.2}Mo$ (Fig. 8a) and $TiZrHfCo_{0.07}Cr_{0.07}Mo$ (Fig. 8b) bio-HEAs were similar to those of the other bio-HEAs including the equiatomic TiNbTaZrMo bio-HEA [15–17], non-equiatomic $Ti_{2.6}NbTaZrMo$ [17], $Ti_{1.4}Zr_{1.4}Nb_{0.6}Ta_{0.6}Zr_{0.6}$, $Ti_{1.7}NbTaZrMo_{0.5}$, and $Ti_{1.5}NbTaZrMo_{0.5}$ bio-HEAs [18].

Fig. 8 shows an elemental map for the as-cast $TiZrHfCr_{0.2}Mo$ bio-HEA obtained using EPMA-WDS. Cr enrichment was observed in the inter-dendrite region in both low- (Fig. 8a) and high- (Fig. 8b) magnification images. The elemental distribution of Ti, Zr, and Mo was not homogeneous. Recently, a eutectic structure in the inter-dendrite region was reported for Laves phase formation-type multi-component Ti-based alloys [57,58]. This implies eutectic-like structure formation in the

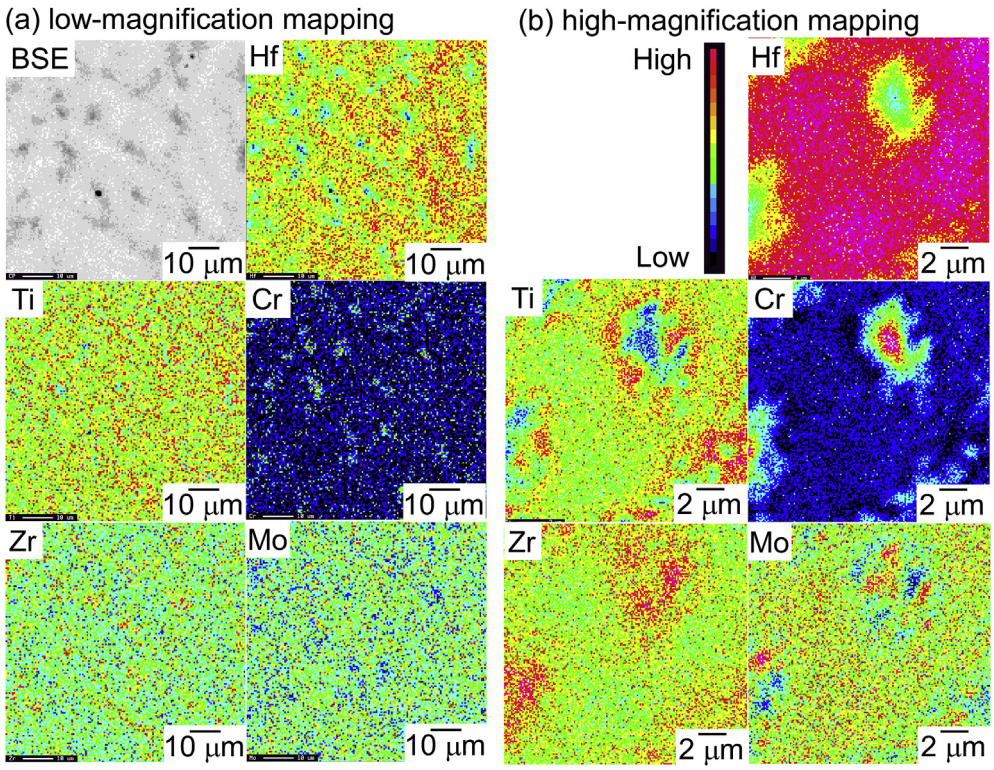

Fig. 8. Elemental mapping of the as-cast $TiZrHfCr_{0.2}Mo$ bio-HEA via EPMA-WDS analysis. (a) low-magnification mapping, (b) high-magnification mapping.

inter-dendrite region in the $TiZrHfCr_{0.2}Mo$ bio-HEA; however, formation of the eutectic-like structure was not clearly determined because of the lack of spatial resolution of the thermionic-emission gun type EPMA used in the present study, similar to the case for the SEM observation. The thermodynamic calculation results of a k at T_L of $TiZrHfCo_{0.2}Mo$ in Table 1 show that the k at T_L of Cr was less than unity, indicating the rejection of Cr from the dendrite phase to the residual liquid and the enrichment of the inter-dendrite region during solidification. There was no discrepancy in the Cr-rich phase formation between the experimental observation and thermodynamic calculation.

Fig. 9 shows an elemental map for the as-cast $TiZrHfCo_{0.07}Cr_{0.07}Mo$ bio-HEA obtained using EPMA-WDS, while Table 2 shows composition analytical results (at.%). A slight enrichment in Mo element was observed at the main dendrite region (denoted as D), compared to the inter-dendrite region. On the other hand, enrichments in Co and Cr elements were clearly observed at the inter-dendrite region (B2). Table 2 summarizes the EPMA-WDS composition analysis results at the dendrite region (denoted as D in Fig. 9) and Co–Cr-enriched inter-dendrite region (denoted as B2 in Fig. 9). The main-dendrite region (D) contained all of the main constituent elements (Ti, Zr, Hf, and Mo), which indicates the formation of the BCC solid solution phase with multi-component elements. The Co–Cr-enriched phase formation was detected in the EPMA elemental mapping (Fig. 9) and EPMA-WDS composition analysis (Table 2). The thermodynamic calculation results of the value of k at T_L of $TiZrHfCo_{0.07}Cr_{0.07}Mo$ in Table 2 shows that k at T_L of Co, Cr and Zr was less than unity, indicating the rejection of these element from dendrite phase to residual liquid and the enrichment of the inter-dendrite region during the solidification. The observed elemental distribution was roughly consistent with the thermodynamic calculation results. The Co–Cr-enriched region contained large amounts of Ti, Zr, Hf, and Mo elements.

The mechanical properties of the as-cast $TiZrHfCr_{0.2}Mo$ and $TiZrHfCo_{0.07}Cr_{0.07}Mo$ bio-HEAs were mainly evaluated using the micro Vickers hardness (Hv) test. The preliminary test for the compression test of the arc-melted ingot showed that the yield stress was approximately

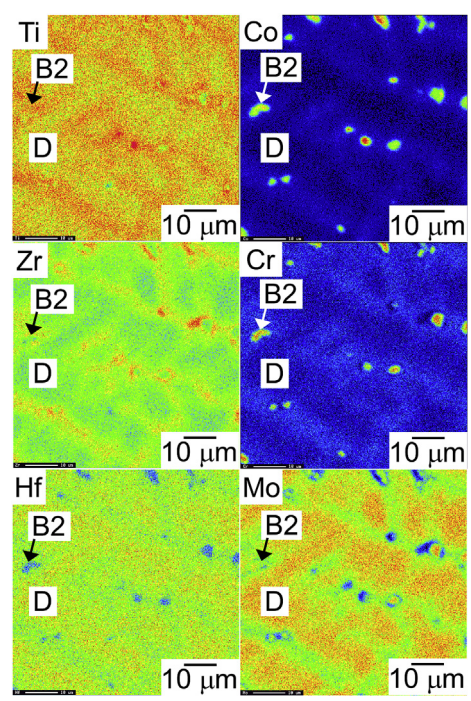

Fig. 9. Elemental mapping of the as-cast $TiZrHfCo_{0.07}Cr_{0.07}Mo$ bio-HEA via EPMA-WDS analysis.

1250 MPa. Fig. 10 shows the Vickers hardness (Hv) values of ingots of the various HEAs: the $TiZrHfCr_{0.2}Mo$ bio-HEA (blue open square, □); the $TiZrHfCo_{0.07}Cr_{0.07}Mo$ bio-HEA (red open circle, ○); and equiatomic TiNbTaZrX (X = V, Mo, W) HEAs (black filled square, ■) including the equiatomic TiNbTaZrMo bio-HEA; the equiatomic TiNbTaZr MEA (black filled circle, ●). Table 3 shows the Hv values of the alloys, in which the average (Av.) and standard deviation (Std.) were obtained

Table 2
EPMA-WDS composition analysis results at the dendrite region (C in Fig. 9) and Co–Cr-enriched inter-dendrite region (B2 in Fig. 9).

Dendrite (index D), at.%					
Ti	Zr	Hf	Co	Cr	Mo
25.9	19.2	26.6	1.2	1.5	25.7
Inter-dendrite (index B2), at.%					
Ti	Zr	Hf	Co	Cr	Mo
25.4	19.6	15.4	14.7	6.9	17.5

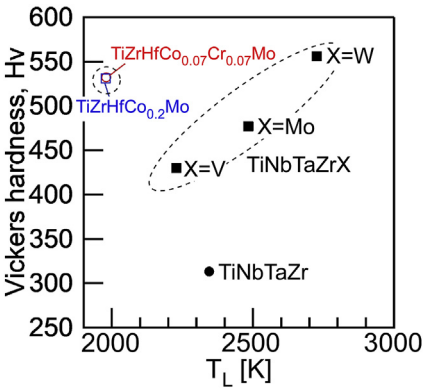

Fig. 10. Vickers hardness values of various as-cast HEAs: $TiZrHfCr_{0.2}Mo$ bio-HEA (blue open squares, □); $TiZrHfCo_{0.07}Cr_{0.07}Mo$ bio-HEA (red open circles, ○); TiNbTaZr bio-MEA (black filled circles, ●); and TiNbTaZrX (X = V, Mo, W) HEAs (black filled squares, ■), including TiNbTaZrMo bio-HEAs. The Vickers hardness is plotted against the liquidus temperature (T_L) estimated by thermodynamic calculations. (For interpretation of the references to colour in this figure legend, the reader is referred to the Web version of this article.)

Table 3
Vickers hardness values of various as-cast HEAs: $TiZrHfCr_{0.2}Mo$ bio-HEA, $TiZrHfCo_{0.07}Cr_{0.07}Mo$ bio-HEA, TiNbTaZr bio-MEA, and TiNbTaZrX (X = V, Mo, W) HEAs including TiNbTaZrMo bio-HEAs. The average (Av.) and standard deviation (Std.) were obtained from at least 10 measurements, the positions for which were randomly selected.

Alloys	T_L [K]	Hv (Av.)	Std.
TiNbTaZr	2346	313	8.8
TiNbTaZrV	2228	430	5.0
TiNbTaZrMo	2484	477	7.8
TiNbTaZrW	2726	556	6.3
$TiZrHfCr_{0.2}Mo$	1980	531	11
$TiZrHfCo_{0.07}Cr_{0.07}Mo$	1978	532	5.9

from at least 10 measurements, the positions for which were randomly selected. The *H*v values were considered to be the hardness, including the effect of Laves phases at the inter-dendrite region. In Fig. 10, the *H*v was plotted against T_L. The *H*v values of the five-component equiatomic TiNbTaZrX (X = V, Mo, W) HEAs were significantly higher than that of the four-component equiatomic TiNbTaZr MEA. The *H*v values of the five-component equiatomic TiNbTaZrX (X = V, Mo, W) HEAs increased monotonously with increasing T_L. The *H*v values of the $TiZrHfCr_{0.2}Mo$ and $TiZrHfCo_{0.07}Cr_{0.07}Mo$ bio-HEAs were higher than that of the equiatomic TiNbTaZrMo bio-HEA, even though the T_L values of the $TiZrHfCr_{0.2}Mo$ and $TiZrHfCo_{0.07}Cr_{0.07}Mo$ bio-HEAs were significantly lower than that of the equiatomic TiNbTaZrMo bio-HEA. The reason for the significantly higher hardness of the $TiZrHfCr_{0.2}Mo$ and $TiZrHfCo_{0.07}Cr_{0.07}Mo$ bio-HEAs is not clear at present. This higher hardness may be explained by the severe lattice distortion caused by the

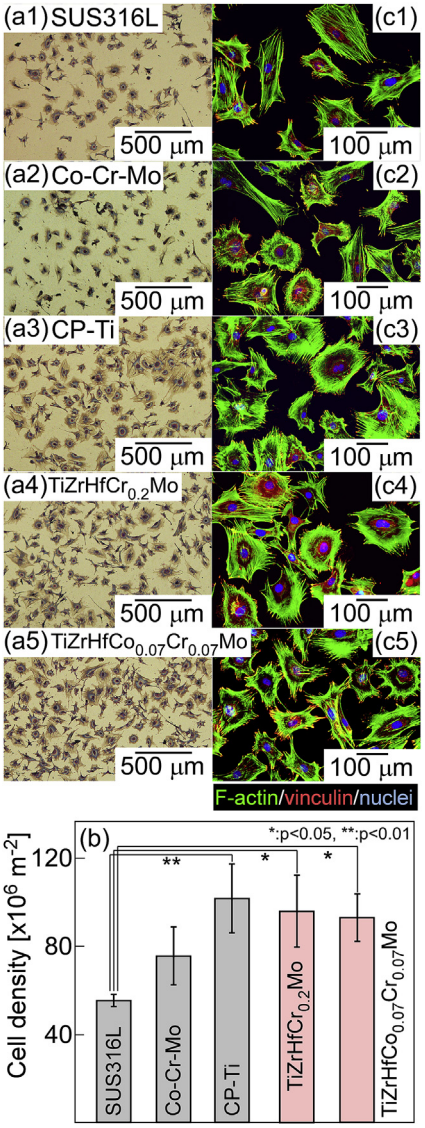

Fig. 11. Biocompatibility analysis results of arc-melted ingots of $TiZrHfCr_{0.2}Mo$ and $TiZrHfCo_{0.07}Cr_{0.07}Mo$ bio-HEAs. (a) Giemsa staining images of osteoblasts cultured on fabricated specimens of SUS316L (stainless steel, JIS SUS316L [60]), CP-Ti, Co–Cr–Mo alloy (wrought cobalt–28chromium–6molybdenum alloys for surgical implants, ASTM F1537-08 [38]), equiatomic TiNbTaZrMo, and $TiZrHfCr_{0.2}Mo$ and $TiZrHfCo_{0.07}Cr_{0.07}Mo$ bio-HEAs. (b) Quantitative analysis of cell density on fabricated specimens. (c) Fluorescent images of osteoblast adhesion on fabricated specimens of SUS316, CP-Ti, Co–Cr–Mo alloy, equiatomic TiNbTaZrMo, and $TiZrHfCr_{0.2}Mo$ and $TiZrHfCo_{0.07}Cr_{0.07}Mo$ bio-HEAs.

formation of the multi-component BCC phase in the main dendritic region and/or dispersion of the Laves phase in the inter-dendrite region. The dispersion of small fractions of Laves phases has been reported to be sufficient to significantly enhance the hardness values in multi-component Ti-based alloys with a BCC phase [57–59]. The present experimental results may imply that the dispersion of a small fraction of Laves phases is effective in increasing the hardness of a BCC type bio-HEAs as well as BCC-type Ti-based alloys [57–59]. Notably, the novel high-strength $TiZrHfCr_{0.2}Mo$ and $TiZrHfCo_{0.07}Cr_{0.07}Mo$ bio-HEAs, whose liquidus temperatures were significantly lower than those of previously reported equiatomic and non-equiatomic TiNbTaZrMo bio-HEAs [15–19], were successfully designed and developed in the present study.

Fig. 11 shows the biocompatibility evaluation results of the alloys.

Specifically, Fig. 11a shows the Giemsa staining images of osteoblasts cultivated for 24 h on fabricated specimens of stainless steel (SUS316L) [56] (Fig. 11a1), Co–Cr–Mo alloy (ASTM F1537-08) [38] (Fig. 11a2), commercial-purity Ti (CP–Ti; Fig. 11a3), $TiZrHfCr_{0.2}Mo$ (Fig. 11a4), and $TiZrHfCo_{0.07}Cr_{0.07}Mo$ (Fig. 11a5). The cell density of SUS316L (Fig. 11a1) was lower than those of CP-Ti (Fig. 11a3), $TiZrHfCr_{0.2}Mo$ (Fig. 11a4) and $TiZrHfCo_{0.07}Cr_{0.07}Mo$ (Fig. 11a5). Quantitative analysis results of the cell density are shown in Fig. 11b (asterisks indicate the statistically significant difference between the two groups). The cell density was strongly dependent on the composition of the alloys: the cell density of SUS316L was clearly lower than that of CP-Ti and the ingots of $TiZrHfCr_{0.2}Mo$, and $TiZrHfCo_{0.07}Cr_{0.07}Mo$. There was no statistical difference between CP-Ti and the developed bio-HEAs. Our previous work demonstrated that the TiNbTaZrMo bio-HEA shows good biocompatibility comparable to that of CP-Ti [15], indicating that the newly developed $TiZrHfCr_{0.2}Mo$ and $TiZrHfCo_{0.07}Cr_{0.07}Mo$ show the same degree of cytocompatibility as that of other bio-HEAs involving TiNbTaZrMo. Along with cell density, the morphology of osteoblasts on a biomaterial is an important indicator as cell spreading plays a significant role in cellular functions involving tissue regeneration. Fig. 11c shows fluorescent images of osteoblast adhesion on the fabricated specimens. The osteoblasts on SUS316L (Fig. 11c1) and the Co–Cr–Mo alloy (Fig. 11c2) were relatively small and less spread out. In contrast, those on $TiZrHfCr_{0.2}Mo$ (Fig. 11c4) and $TiZrHfCo_{0.07}Cr_{0.07}Mo$ (Fig. 11c5) showed a widespread morphology, almost similar to the morphology of the cells on CP-Ti (Fig. 11c3). This indicates that the $TiZrHfCr_{0.2}Mo$ and $TiZrHfCo_{0.07}Cr_{0.07}Mo$ bio-HEAs are much more advantageous than SUS316L and the Co–Cr–Mo alloy for bone tissue compatibility. It was clarified that the osteoblasts on $Ti_{1.4}Zr_{1.4}Nb_{0.6}Ta_{0.6}Mo_{0.6}$ bio-HEA possess significantly longer structures of fibrillar adhesion compared to $Ti_{0.6}Zr_{0.6}Nb_{1.4}Ta_{1.4}Mo_{1.4}$ bio-HEA, indicating that Ti–Nb–Ta–Zr–Mo bio-HEA stimulated the maturation of focal adhesion plaques in osteoblasts [18]. The maturation of focal adhesion, as well as cell alignment, is closely related to the functional organization of biological tissue around the implanted biomaterials [61–63]. The development of the wide-spread morphology of the cells on the $TiZrHfCr_{0.2}Mo$ and $TiZrHfCo_{0.07}Cr_{0.07}Mo$ bio-HEAs may lead to the superior biocompatibility of these newly developed bio-HEAs; the interaction of cells and $TiZrHfCr_{0.2}Mo$ and $TiZrHfCo_{0.07}Cr_{0.07}Mo$ bio-HEAs will be clarified in future studies. The combination of a Ti- and Zr-based oxide layer in a Ti–Nb–Ta–Zr alloy has been shown to have excellent biocompatibility [64]. Furthermore, a Ti–30Zr–7Mo alloy was reported to have shown a significantly increased number of cells as compared to that of CP-Ti, allowing for the formation of Zr-and Ti-based oxide layers [65]. Taken together, the excellent biocompatibility in $TiZrHfCr_{0.2}Mo$ and $TiZrHfCo_{0.07}Cr_{0.07}Mo$ bio-HEAs may be because of the particular oxide layer based on the complicated arrangement of the constituent metallic elements. The application of the developed bio-HEAs as biomedical materials should be investigated strictly on the basis of biological analysis regarding the functional interaction between materials and cells; research involving gene expression analysis is now in progress. Finally, it can be emphasized that the present results are the first to demonstrate the excellent biocompatibility of Ti–Zr–Hf–Cr–Mo and Ti–Zr–Hf–Co–Cr–Mo bio-HEAs, which is comparable to that of CP-Ti.

5. Conclusions

In conclusion, this study developed $TiZrHfCr_{0.2}Mo$ and $TiZrHfCo_{0.07}Cr_{0.07}Mo$ bio-HEAs. $TiZrHfCr_{0.2}Mo$ and $TiZrHfCo_{0.07}Cr_{0.07}Mo$ bio-HEAs were designed using (a) a treelike diagram for alloy development, (b) empirical alloy parameters for solid-solution-phase formation, and (c) thermodynamic calculations focused on solidification. The liquidus temperatures of the $TiZrHfCr_{0.2}Mo$ and $TiZrHfCo_{0.07}Cr_{0.07}Mo$ bio-HEAs were estimated to be 1978 K (1705 °C) and 1980 K (1707 °C), respectively, which are much below 2273 K (2000 °C). The ingots of the $TiZrHfCr_{0.2}Mo$ and $TiZrHfCo_{0.07}Cr_{0.07}Mo$ bio-HEAs showed equiaxed dendrites with BCC structures. The ingots of these two bio-HEAs also showed higher Vickers hardness than the equiatomic TiNbTaZrMo bio-HEA. Both these bio-HEAs showed excellent biocompatibility comparable to that of CP-Ti. The development of $TiZrHfCr_{0.2}Mo$ and $TiZrHfCo_{0.07}Cr_{0.07}Mo$ bio-HEAs with excellent biocompatibility comparable to that of commercial-purity Ti provides authenticity of the application of bio-HEAs for orthopedic implants with multiple functions.

Declaration of competing interest

The authors declare no conflicts of interest associated with this manuscript.

Acknowledgment

This study was partially supported by JSPS KAKENHI (grant numbers 17H06224, 18H05254, 18K04750, 18H05455, and 19H05172); the Council for Science, Technology and Innovation (CSTI); the Cross-Ministerial Strategic Innovation Promotion Program (SIP); and the Innovative Design/Manufacturing Technologies program (Establishment and Validation of the Base for 3D Design and Additive Manufacturing Standing on the Concepts of “Anisotropy” and “Customization”) of the New Energy and Industrial Technology Development Organization (NEDO). The authors are grateful to Prof. T. Tanaka and Prof. M. Suzuki at Osaka University for their help with the thermodynamic calculations.

Appendix A. Supplementary data

Supplementary data to this article can be found online at https://doi.org/10.1016/j.msec.2019.110322.

Author rules

T. Nagase: Investigation, Writing - original draft.
Y. Iijima: Investigation.
A. Matsugaki: Investigation, Writing - original draft.
K. Ameyama: Investigation.
T. Nakano: Supervision, Writing - review & editing.

References

[1] B. Cantor, I.T.H. Chang, P. Knight, A.J.B. Vincent, Microstructural development in equiatomic multicomponent alloys, Mater. Sci. Eng. A 375–377 (2004) 213–218, https://doi.org/10.1016/j.msea.2003.10.257.
[2] J.W. Yeh, S.K. Chen, S.J. Lin, J.Y. Gan, T.S. Chin, T.T. Shun, C.H. Tsau, S.Y. Chang, Nanostructured high-entropy alloys with multiple principal elements: novel alloy design concepts and outcomes, Adv. Eng. Mater. 6 (2004) 299–303, https://doi.org/10.1002/adem.200300567.
[3] S. Ranganathan, Alloyed pleasures: multimetallic cocktails, Curr. Sci. 85 (2003) 1404–1406 https://www.currentscience.ac.in/Downloads/article_id_085_10_1404_1406_0.pdf.
[4] Y. Zhang, Y.J. Zhou, J.P. Lin, G.L. Chen, P.K. Liew, Solid-solution phase formation rules for multi-component alloys, Adv. Eng. Mater. 10 (2008) 534–538, https://doi.org/10.1002/adem.200700240.
[5] J.W. Yeh, Alloy design strategies and future trends in high-entropy alloys, J. Occup. Med. 65 (2013) 1759–1771, https://doi.org/10.1007/s11837-013-0761-6.
[6] M.H. Tsai, J.W. Yeh, High-entropy alloys: a critical review, Mater. Res. Lett. 2 (2014) 107–123, https://doi.org/10.1080/21663831.2014.912690.
[7] Y. Zhang, T.T. Zuo, Z. Tang, M.C. Gao, K.A. Dahmen, P.K. Liaw, Z.P. Lu, Microstructures and properties of high-entropy alloys, Prog. Mater. Sci. 61 (2014) 1–93, https://doi.org/10.1016/j.pmatsci.2013.10.001.
[8] B.S. Murty, J.-W. Yeh, S. Ranganathan, High-Entropy Alloys, first ed., Elsevier, 2014.
[9] M.C. Gao, J.-W. Yeh, P.K. Liaw, Y. Zhang, High-Entropy Alloys, Fundamentals and Applications, first ed., Springer, 2016.
[10] Y.F. Ye, Q. Wang, J. Lu, C.T. Liu, Y. Yang, High-entropy alloy: challenges and prospects, Mater. Today 19 (2016) 349–362, https://doi.org/10.1016/j.mattod.2015.11.026.
[11] D.B. Miracle, O.N. Senkov, A critical review of high entropy alloys and related concepts, Acta Mater. 122 (2017) 448–511, https://doi.org/10.1016/j.actamat.2016.08.081.

[12] T. Nagase, Development of high entropy alloys as the casting alloys, J. of the Society of Mechanical Engineers 121 (2018) 8–11, https://doi.org/10.1299/jsmemag.121.1192_8.
[13] W. Zhang, P.K. Liew, Y. Zhang, Science and technology in high-entropy alloys, Sci. China Mater. 61 (2018) 2–22, https://doi.org/10.1007/s40843-017-9195-8.
[14] D.B. Miracle, High entropy alloys as a bold step forward in alloy development, Nat. Commun. 10 (2019) 1805, https://doi.org/10.1038/s41467-019-09700-1.
[15] M. Todai, T. Nagase, T. Hori, A. Matsugaki, A. Sekita, T. Nakano, Novel TiNbTaZrMo high-entropy alloys for metallic biomaterials, Scr. Mater. 129 (2017) 65–68, https://doi.org/10.1016/j.scriptamat.2016.10.028.
[16] T. Nagase, K. Mizuuchi, T. Nakano, Solidification microstructures of the ingots obtained by arc melting and cold crucible levitation melting in TiNbTaZr medium-entropy alloy and TiNbTaZrX (X = V, Mo, W) high-entropy alloys, Entropy 21 (2019) 483, https://doi.org/10.3390/e21050483.
[17] T. Nagase, M. Todai, T. Hori, T. Nakano, Microstructure of equiatomic and non-equiatomic Ti-Nb-Ta-Zr-Mo high-entropy alloys for metallic biomaterials, J. Alloy. Comp. 753 (2018) 412–421, https://doi.org/10.1016/j.jallcom.2018.04.082.
[18] T. Hori, T. Nagase, M. Todai, A. Matsugaki, T. Nakano, Development of non-equiatomic Ti-Nb-Ta-Zr-Mo high-entropy alloys for metallic biomaterials, Scr. Mater. 172 (2019) 83–87, https://doi.org/10.1016/j.scriptamat.2019.07.011.
[19] S.P. Wang, J. Xu, TiZrNbTaMo high-entropy alloy designed for orthopedic implants: as-cast microstructure and mechanical properties, Mater. Sci. Eng. C73 (2017) 80–89, https://doi.org/10.1016/j.msec.2016.12.057.
[20] Y. Yuan, Y. Wu, Z. Yang, X. Liang, Z. Lei, H. Huang, H. Wang, X. Liu, K. An, W. Wu, Z. Lu, Formation, structure and properties of biocompatible TiZrHfNbTa high-entropy alloys, Mater. Res. Lett. 7 (2019) 225–231, https://doi.org/10.1080/21663831.2019.1584592.
[21] A. Motallebzadeh, N.S. Peighambardoust, S. Sheikh, H. Murakami, S. Guo, D. Canadinc, Microstructural, mechanical and electrochemical characterization of TiZrTaHfNb and Ti1.5ZrTa0.5Hf0.5Nb0.5 refractory high-entropy alloys for biomedical applications, Intermetallics 113 (2019) 106572, https://doi.org/10.1016/j.intermet.2019.106572.
[22] G. Popescu, B. Ghiban, C.A. Popescu, L. Rosu, R. Trusca, I. Carcea, V. Soare, D. Dumitrescu, I. Constantin, M.T. Olaru, B.A. Carlan, New TiZrNbTaFe high entropy alloy used for medical applications, IOP Conf. Series 400 (2018) 022049, , https://doi.org/10.1088/1757-899X/400/2/022049.
[23] V.T. Nguyen, M. Qian, Z. Shi, T. Song, L. Huang, J. Zou, A novel quaternary equiatomic Ti-Zr-Nb-Ta medium entropy alloy (MEA), Intermetallics 101 (2018) 39–43, https://doi.org/10.1016/j.intermet.2018.07.008.
[24] O.N. Senkov, G.B. Wilks, D.B. Miracle, C.P. Chuang, P.K. Liaw, Refractory high-entropy alloys, Intermetallics 18 (2010) 1758–1765, https://doi.org/10.1016/j.intermet.2010.05.014.
[25] O.N. Senkov, G.B. Wilks, J.M. Scott, D.B. Miracle, Mechanical properties of Nb25Mo25Ta25W25 and V20Nb20Mo20Ta20W20 refractory high entropy alloys, Intermetallics 19 (2011) 698–706, https://doi.org/10.1016/j.intermet.2011.01.004.
[26] O.N. Senkov, J.M. Scotta, S.V. Senkova, D.B. Miracle, C.F. Woodward, Microstructure and room temperature properties of a high-entropy TaNbHfZrTi alloy, J. Alloy. Comp. 509 (2011) 6043–6048, https://doi.org/10.1016/j.jallcom.2011.02.171.
[27] O.N. Senkov, J.M. Scott, S.V. Senkova, F. Meisenkothen, D.B. Miracle, C.F. Woodward, Microstructure and elevated temperature properties of a refractory TaNbHfZrTi alloy, J. Mater. Sci. 47 (2012) 4062–4074, https://doi.org/10.1007/s10853-012-6260-2.
[28] O.N. Senkov, D.B. Miracle, K.J. Chaput, J.-P. Couzinie, Development and exploration of refractory high entropy alloys-A review, J. Mater. Res. 33 (2018) 3092–3128, https://doi.org/10.1557/jmr.2018.153.
[29] T. Nagase, S. Anada, P.D. Rack, J.H. Noh, H. Yasuda, H. Mori, T. Egami, MeV electron-irradiation-induced structural change in the bcc phase of Zr-Hf-Nb alloy with an approximately equiatomic ratio, Intermetallics 38 (2013) 70–79, https://doi.org/10.1016/j.intermet.2013.02.009.
[30] T. Nagase, S. Anada, P.D. Rack, J.H. Noh, H. Yasuda, H. Mori, T. Egami, Electron-irradiation-induced structural change in Zr-Hf-Nb alloy, Intermetallics 26 (2012) 122–130, https://doi.org/10.1016/j.intermet.2012.02.015.
[31] T.M. Devine, F.J. Kummer, Wrought cobalt-chromium surgical implant alloys, J. Wulff, J. Mater. Sci. 7 (1972) 126–128, https://doi.org/10.1007/BF00549560.
[32] T.M. Devine, J. Wulff, Cast vs. wrought cobalt-chromium surgical implant alloys, J. Biomed. Mater. Res. 9 (1975) 151–167, https://doi.org/10.1002/jbm.820090205.
[33] J. Cohen, R.M. Rose, J. Wulff, Recommended heat treatment and alloy additions for cast Co-Cr surgical implants, J. Biomed. Mater. Res. 12 (1978) 935–937, https://doi.org/10.1002/jbm.820120613.
[34] T. Kilner, R.M. Pilliar, G.C. Weatherly, C. Alibert, Phase identification and incipient melting in a cast Co-Cr surgical implant alloy, J. Biomed. Mater. Res. 16 (1982) 63–79, https://doi.org/10.1002/jbm.820160109.
[35] M. Niinomi, Recent metallic materials for biomedical applications, Metall. Mater. Trans. A 33 (2002) 477–486, https://doi.org/10.1007/s11661-002-0109-2.
[36] M. Niinomi, M. Nakai, J. Hieda, Development of new metallic alloys for biomedical applications, Acta Biomater. 8 (2012) 3888–3903, https://doi.org/10.1016/j.actbio.2012.06.037.
[37] ASTM F75, https://www.astm.org/Standards/F75 , Accessed date: 17 September 2018.
[38] ASTM F1537-08, https://www.astm.org/Standards/F1537.htm , Accessed date: 16 May 2019.
[39] JIS T 7402, http://www.jisc.go.jp/eng/index.html , Accessed date: 17 September 2018.
[40] M. Niinomi, Design and development of metallic biomaterials with biological and mechanical biocompatibility, J. Biomed. Mater. Res. A 107 (2019) 944–954, https://doi.org/10.1002/jbm.a.36667.
[41] H. Matsuno, A. Yokoyama, F. Watari, M. Uo, T. Kawasaki, Biocompatibility and osteogenesis of refractory metal implants, titanium, hafnium, niobium, tantalum and rhenium, Biomaterials 22 (2001) 1253–1262, https://doi.org/10.1016/S0142-9612(00)00275-1.
[42] B.L. Wang, L. Li, Y.F. Zheng, In vitro cytotoxicity and hemocompatibility studies of Ti-Nb, Ti-Nb-Zr and Ti-Nb-Hf biomedical shape memory alloys, Biomed. Mater. 5 (2010) 044102, , https://doi.org/10.1088/1748-6041/5/4/044102.
[43] T. Hanawa, Techniques improving reliability of metals in the human body, J. Surf. Finish. Soc. Jpn. 58 (2007) 495–499, https://doi.org/10.4139/sfj.58.495.
[44] S. Sheikh, S. Shafeie, Q. Hu, J. Ahlstrom, C. Persson, J. Vesely, J. Zyka, U. Klement, S. Guo, Alloy design for intrinsically ductile refractory high-entropy alloys, J. Appl. Phys. 120 (2016) 164902, https://doi.org/10.1063/1.4966659.
[45] C.D. Rabadia, Y.J. Liu, G.H. Cao, Y.H. Li, C.W. Zhang, T.B. Sercombe, H. Sun, L.C. Zhang, High-strength b stabilized Ti-Nb-Fe-Cr alloys with large plasticity, Mater. Sci. Eng., A 732 (2018) 368–377, https://doi.org/10.1016/j.msea.2018.07.031.
[46] S.F. Jawed, C.D. Rabadia, Y.J. Liu, L.Q. Wang, Y.H. Li, X.H. Zhang, L.C. Zhang, Mechanical characterization and deformation behavior of b-stabilized Ti-Nb-Sn-Cr alloys, J. Alloy. Comp. 792 (2019) 684–693, https://doi.org/10.1016/j.jallcom.2019.04.079.
[47] L.-C. Zhang, L. Yu Chen, A review on biomedical titanium alloys: recent progress and prospect, Adv. Eng. Mater. 21 (2019) 1801215, https://doi.org/10.1002/adem.201801215.
[48] L.-C. Zhang, Y. Liu, S. Li, Y. Hao, Additive manufacturing of titanium alloys by electron beam melting: a review, Adv. Eng. Mater. 20 (2018) 1700842, https://doi.org/10.1002/adem.201700842.
[49] T. Nagase, T. Hori, M. Todai, S.-H. Sun, T. Nakano, Materials & Design vol. 173, (2019), pp. 107771 1–10777110. Additive manufacturing of dense components in beta-titanium alloys with crystallographic texture from a mixture of pure metallic element powders.
[50] X. Yang, Y. Zhang, Prediction of high-entropy stabilized solid-solution in multi-component alloys, Mater. Chem. Phys. 132 (2012) 233–238, https://doi.org/10.1016/j.matchemphys.2011.11.021.
[51] A. Takeuchi, A. Inoue, Classification of bulk metallic glasses by atomic size difference, heat of mixing and period of constituent elements and its application to characterization of the main alloying element, Mater. Trans. 46 (2005) 2817–2829, https://doi.org/10.2320/matertrans.46.2817.
[52] T. Nagase, K. Mizuuchi, M. Todai, T. Nakano, Solidification microstructure of high entropy alloys composed with 4 group (Ti, Zr, Hf), 5 group (V, Nb, Ta), and 6 group (Cr, Mo, W) elements, Materia Japan 58 (2019) 78, https://doi.org/10.2320/materia.58.78.
[53] C.W. Bale, A.D. Pelton, W.T. Thompson, G. Eriksson, FactSage, ecole poly-technique, Montreal (2001), http://www.crct.polymtl.ca , Accessed date: 10 October 2018.
[54] T. Nagase, M. Matsumoto, Y. Fujii, Microstructure of Ti-Ag immiscible alloys with metastable liquid phase separation, J. Alloy. Comp. 738 (2018) 440–447, https://doi.org/10.1016/j.jallcom.2017.12.138.
[55] T. Nagase, M. Takemura, M. Matsumuro, T. Maruyama, Solidification microstructure analysis of $AlCoCrFeNi_{2.1}$ eutectic high entropy alloy ingots, Mater. Trans. 59 (2018) 255–264, https://doi.org/10.2320/matertrans.F-M2017851.
[56] T. Nagase, A. Shibata, M. Matsumuro, M. Takemura, S. Semboshi, Alloy design and fabrication of ingots in Cu-Zn-Mn-Ni-Sn high-entropy and Cu-Zn-Mn-Ni medium-entropy brasses, Mater. Des. 181 (2019) 107900 1–9, https://doi.org/10.1016/j.matdes.2019.107900 2019.
[57] C.D. Rabadia, Y.J. Liu, L. Wang, H. Sun, L.C. Zhang, Laves phase precipitation in Ti-Zr-Fe-Cr alloys with high strength and large plasticity, Mater. Des. 154 (2018) 228–238, https://doi.org/10.1016/j.matdes.2018.05.035.
[58] C.D. Rabadia, Y.J. Liu, S.F. Jawed, L. Wang, Y.H. Li, X.H. Zhang, T.B. Sercombe, H. Sun, L.C. Zhang, Improved deformation behavior in Ti-Zr-Fe-Mn alloys comprising the C14 type Laves and b phases, Mater. Des. 160 (2018) 1059–1070, https://doi.org/10.1016/j.matdes.2018.10.049.
[59] C.D. Rabadia, Y.J. Liu, L.Y. Chen, S.F. Jawed, L.Q. Wang, H. Sun, L.C. Zhang, Deformation and strength characteristics of Laves phases in titanium alloys, Mater. Des. 179 (2019) 107891 1–9, https://doi.org/10.1016/j.matdes.2019.107891.
[60] JIS SUS316L, http://www.jssa.gr.jp/contents/products/standards/jis/austenite/ , Accessed date: 16 May 2019.
[61] Y. Nakanishi, A. Matsugaki, K. Kawahara, T. Ninomiya, H. Sawada, T. Nakano, Unique arrangement of bone matrix orthogonal to osteoblast alignment controlled by Tspan11-mediated focal adhesion assembly, Biomaterials 209 (2019) 103–110, https://doi.org/10.1016/j.biomaterials.2019.04.016.
[62] A. Matsugaki, G. Aramoto, T. Ninomiya, H. Sawada, S. Hata, T. Nakano, Abnormal arrangement of a collagen/apatite extracellular matrix orthogonal to osteoblast alignment is constructed by a nanoscale periodic surface structure, Biomaterials 37 (2015) 134–143, https://doi.org/10.1016/j.biomaterials.2014.10.025.
[63] A. Matsugaki, N. Fujiwara, T. Nakano, Continuous cyclic stretch induces osteoblast alignment and formation of anisotropic collagen fiber matrix, Acta Biomater. 9 (2013) 7227–7235, https://doi.org/10.1016/j.actbio.2013.03.015.
[64] X. Zhao, M. Niinomi, M. Nakai, J. Hieda, T. Ishimoto, T. Nakano, Optimization of Cr content of metastable β-type Ti-Cr alloys with changeable Young's modulus for spinal fixation applications, Acta Biomater. 8 (2012) 2392–2400, https://doi.org/10.1016/j.actbio.2012.02.010.
[65] X. Zhao, M. Niinomi, M. Nakai, T. Ishimoto, T. Nakano, Development of high Zr-containing Ti-based alloys with low Young's modulus for use in removable implants, Mater. Sci. Eng. C 31 (2011) 1436–1444, https://doi.org/10.1016/j.msec.2011.05.013.